Giant photoelectric energy conversion via a 3C-SiC Nano-Thin film double heterojunction

Dinh Gia Ninh [a,b,g,*], Minh Tam Hoang [c,d], Tony Wang [e], Tuan-Hung Nguyen [a],
Tuan-Khoa Nguyen [a], Erik Streed [f], Hongxia Wang [c,d], Yong Zhu [b], Nam-Trung Nguyen [a],
Van Dau [b], Dzung Viet Dao [a,b]

[a] Queensland Micro and Nanotechnology Centre (QMNC), Griffith University, Brisbane, QLD 4111, Australia
[b] School of Engineering and Built Environment, Griffith University, Gold Coast, QLD 4215, Australia
[c] School of Chemistry and Physics, Faculty of Science, Queensland University of Technology, Brisbane, QLD 4001, Australia
[d] Centre for Materials Science, Queensland University of Technology (QUT), Brisbane, QLD, 4001, Australia
[e] Central Analytical Research Facility, Queensland University of Technology (QUT), Brisbane, QLD, 4001, Australia
[f] Institute for Glycomics, Griffith University, Southport 4222, Australia
[g] School of Mechanical Engineering, Hanoi University of Science and Technology, Hanoi, 100000, Vietnam

ARTICLE INFO

ABSTRACT

Enhancing the energy conversion efficiency is utmost important in renewable energy and self-powered opto-electronic sensing applications. In this study, we propose the concept of a p-3C-SiC nano-thin film/p-Si/n-Si double junction (DJ) structure, which exhibits a massive photoelectric energy conversion efficiency and ultra-high sensitivity of optoelectronic sensors. The optoelectronic characteristics of this DJ heterostructure are compared to those of a p-3C-SiC/n-Si single-junction (SJ) heterostructure, which shares similarities in all technical and material parameters, except for the inclusion of the middle p-Si layer in the DJ structure. The experimental results reveal that the lateral photocurrent, sensitivity, theoretical power and maximum power of the DJ structure are more than 100 times (i.e. over 10,000%) greater than those of the SJ structure. We then demonstrated these excellent features of DJ heterostructure through developing of a self-powered position sensitive sensor, which showed an ultrahigh sensitivity. The enormous enhancement in the performance has been elucidated through the efficient photogeneration of charge carriers, electron-hole pair splitting, and the improved charge carrier transport mechanisms in the double heterojunction. This research represents a notable breakthrough in ultra-sensitive optoelectronic sensors and photoenergy conversion, since the proposed concept and theoretical model can be extended to multiple junctions of various semiconductor materials.

1. Introduction

1.1. Advantages of double junction and multijunction optoelectronic devices

Renewable energy sources, encompassing solar photovoltaic, wind, hydropower, geothermal energy, and biomass sources, have significantly contributed to the pursuit of carbon neutrality, and the mitigation of global warming and climate change. In particular, solar photovoltaic technology holds significant importance, contributing approximately 24.23 % of total renewable electricity generation, equivalent to 2,587.6 GW [1]. Consequently, optoelectronic devices [2–4] have

emerged as crucial elements within the renewable energy field, serving as an essential conduit for addressing energy-related dilemmas and fostering sustainability in the field of green energy. In addition, natural light (sunlight) is considered a virtually inexhaustible energy source that can be applied in the renewable energy and energy harvesting industries as the world transitions away from fossil fuels. Therefore, the development of self-powered optoelectronic devices, with various applications in energy harvesting [5,6], green energy [7,8], sensors and solar cells [9–12], and robotic industries [13,14], is becoming urgent. High performance characteristics of optoelectronic devices, including high sensitivity, fast response speed and high energy conversion efficiency, are becoming increasingly demanding. To achieve this, new materials

and sophisticated heterostructures, such as multiple layers of different materials stacked on each other, have been investigated, while keeping production costs low. Among these heterostructures, double junction (DJ) heterostructures exhibit many advantages over single junction (SJ) counterparts, such as higher charge carrier generation [15–17], lower recombination rates [17,18], and higher energy conversion efficiency. Furthermore, DJ heterostructures outperform SJ structures in terms of minimizing the major effects of thermal generation (i.e., dark current density) and parasitic impedances [19,20]. DJ heterostructures have been applied effectively in solar cells, where high power conversion efficiency (PCE) is a primary goal. The PCE of solar cells varies with the materials, such as for InGaAsNSb/Ge (9.05 %) [21], a-Si:H/HIT (14.26 %) [22], GaInP/GaAs/Si (16.8 %) [23], GaAs/GaAs//Si II (20.4 %) [24], III-V/Si (32.8 %) [25], and CdTe-DJ (44.14 %) solar cells [26]. In addition, perovskite materials [27–29] have recently emerged as promising materials for optoelectronics applications with a high PCE and a low cost. However, the relentless pursuit of enhancing the PCE in sensing devices and solar cells persists, leaving the PCE of these devices under sunlight illumination still far from achieving true satisfaction.

1.2. Materials used for optoelectronic devices

Identifying the material that yields the highest enhancement in the PCE is an intriguing challenge for researchers. Compared to all other industrial materials, semiconductor materials stand out as preeminent substances, possessing the exceptional capability to efficiently absorb sunlight and convert it into electrical energy. Therefore, the utilization of semiconductor materials featuring diverse energy band structures to engineer optoelectronic devices with varying levels of sensitivity, photocurrents, photovoltages, and maximum power outputs constitutes an intriguing pursuit for researchers in this field. Mustafa et al. [30] theoretically investigated the optoelectronic and transport characteristics of $MgLu_2Z_4$ (Z=S, Se) spinels for energy harvesting applications. Lin et al. [31] reviewed graphene/semiconductor materials for optoelectronic devices to improve performance, and the PCE of the heterostructures could reach 30 %. Zhou et al. [32] investigated transparent and flexible triboelectric nanogenerators that could be applied to many optoelectronic devices supporting finger-or-pen-based touchscreen inputs in self-powered and energy harvesting applications. 2D material advancements have also contributed to the development of optoelectronic devices with improved sensitivity, signal response, and energy harvesting ability [33–36]. The proposed structures demonstrate advantages in terms of optoelectronic properties, however, to the best of the authors' knowledge, there is currently no structure capable of achieving a photocurrent, sensitivity, and maximum power enhancement of over 10,000 % when comparing double heterostructures and single heterostructures under identical conditions. Therefore, researchers still persist in their efforts to find heterostructures for enhanced conversion efficiency surpassing that of current models, and novel structural enhancements to conventional bulk materials (Si, SiC, GaN,…) are still being explored due to their straightforward and cost-effective manufacturing processes.

1.3. Introducing heterostructures and their applications

Silicon carbide (SiC) is an interesting bulk material with excellent mechanical, electrical, and chemical properties that can work well in harsh environments [37,38]. The SiC polytypes 4H-, 6H- and 3C-SiC are frequently employed in microelectromechanical system (MEMS)/nanoelectromechanical system (NEMS) devices [39–41]. 3C-SiC can be directly produced on Si substrates in a cold-wall chemical vapor deposition reactor at temperatures ranging from 1000-1100 °C (below the Si melting point). As a result, the cost of a 3C-SiC wafer is remarkably lower than other polytype wafers (4H-SiC, 6H-SiC) [42]. In addition, with a wide energy bandgap of approximately 2.36 eV and excellent chemical inertness, 3C-SiC is a promising material for optoelectronic devices and can be used under extreme conditions. There are numerous

3C-SiC structures that can be combined with other materials to enable a variety of applications in micro-/nanosystems, including GaN/3C-SiC/Si [43], NbN films/3C-SiC/Si [44], AlN/3C-SiC/Si [45], and AlGaN/GaN/3C-SiC on diamond [46]. However, there has been no previous research on p-3C-SiC/p-Si/n-Si double heterostructures. Moreover, conducting a comprehensive comparative analysis of these two heterostructures under entirely identical conditions represents a novel and pioneering endeavor. The proposed models can be scalable to multiple junctions of various semiconductor materials to increase photoelectric energy conversion efficiency and sensitivity of optoelectronic devices. Potential applications of the above-described devices include the development of a position-sensitive detector (PSD), angle measurements, high-speed trajectory tracking, and vibration frequency measurements, among others [47]. Double-junction or multijunction structures are commonly employed in photodetectors to achieve high performance [48,49]. However, the use of multijunction structures in PSDs, particularly those utilizing bulk materials, remains relatively rare. Notable examples include double-junction asymmetric TiO_2/MoS_2/reduced graphene oxide sandwiches [50], nano-films of $Ti/SrTiO_3$ on p-type silicon [51], and ITO/MoS_2/p-Si structure [52]. Consequently, exploring of the double and multijunction heterostructures for their optoelectronic properties in the PSD applications is a promising and exhilarating avenue of research.

1.4. Summarizing the achievements and advantages of DJ structure compared to SJ structure

In this article, a novel p-3C-SiC/p-Si/n-Si double junction (DJ) structure was designed, and its excellent optoelectronic performance was experimentally and theoretically investigated and compared to that of a p-3C-SiC/n-Si single heterojunction (SJ) structure. For comparison purposes, the material, geometrical, physical, and chemical properties of the p-3C-SiC and n-Si layers in these two heterostructures are identical. The wafers of these materials were fabricated by and purchased from a Japanese semiconductor company based on our designs (details in the **Supporting Information**). The prices of the two types of wafers are almost the same, and the fabrication processes of the devices are identical. However, the experimental results show great advantages for the new p-3C-SiC/p-Si/n-Si DJ structure. The DJ structure exhibits a sensitivity, a lateral photocurrent, a theoretical power (P_T), and a maximum power (P_M) of over 100 times (10,000 %) greater than those of the SJ structure under the same conditions. The unique aspect of the DJ design is that the middle p-Si layer has a smaller resistivity and a higher charge carrier mobility than the p-3C-SiC thin film (detailed in **Supporting Information**). Explanations of the generation and transport mechanisms of charge carriers underlying these interesting physical phenomena are presented in this paper. This work demonstrates the enormous potential for such designed DJ structures in ultrasensitive sensing and high-efficient energy harvesting applications.

2. Materials and structures

2.1. Design of heterostructure

In order to enhance the photovoltaic effect and energy conversion efficiency, we introduce a middle p-Si layer between the p-3C-SiC and n-Si layers to form the p-3C-SiC/p-Si/n-Si DJ as shown in Fig. 1a. The following sections will clarify the underlying rationale for this p-Si layer inclusion. To evaluate the efficiency and advantage of the proposed p-3C-SiC/p-Si/n-Si DJ, a p-3C-SiC/n-Si SJ (Fig. 1b) was also designed and fabricated. The thicknesses of the p-3C-SiC and n-Si layers in both heterostructures are 500 nm and 500 μm, respectively, while that of the middle p-Si layer in the DJ structure is 1 μm. The two metal electrodes on the p-SiC, used to collect the charge carriers, are spaced 500 μm apart with the size of 200 × 1000 μm. The detailed specifications of the two heterostructures including the crystallographic orientation, thickness,
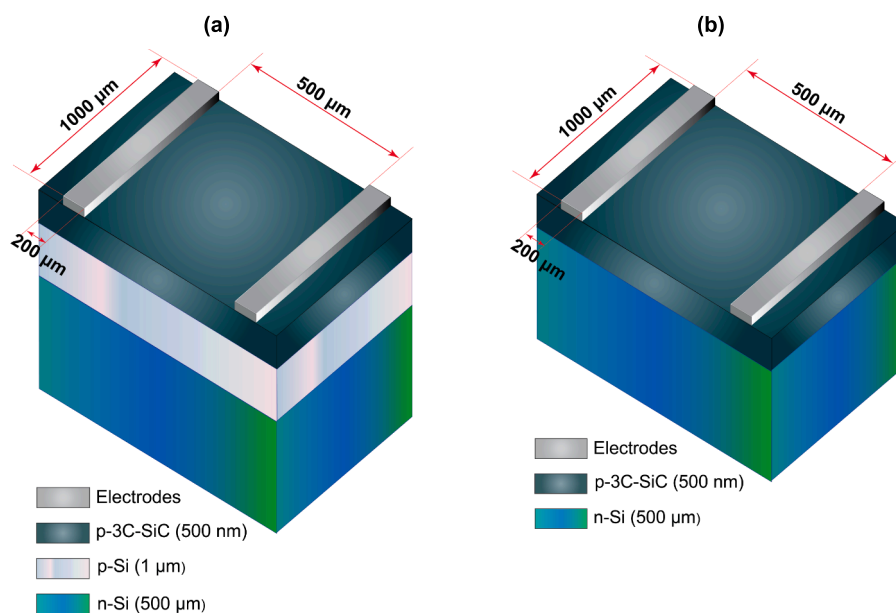
Fig. 1. Schematic of the two heterostructures devices. (a) p-3C-SiC/p-Si/n-Si double junction, (b) p-3C-SiC/n-Si single junction.

semiconductor type, dopant and doping concentration are shown in **Table S1** (Supporting Information). The wafers were fabricated by the D&X Company, which is specializing in semiconductor materials based in Japan, (see Method section). The fabrication process of the two heterostructure devices was carried out as shown in Fig. 8.

2.2. Material and heterostructure characterization

First, material characterization is carried out to confirm the physical and chemical properties of the SJ and DJ heterostructures. The transmission electron microscopy (TEM) images in Fig. 2**a and b** show a SiC layer with a thickness of ~ 500 nm grown on top of the Si substrate. These TEM images were captured by a Hitachi HT 7700 TEM equipped with a tungsten filament operating at 100 kV. To characterize the chemical composition and crystal structure of the heterostructures, X-ray diffraction (XRD), reciprocal space mapping (RSM), and wide-range reciprocal space mapping (WR-RSM) were conducted. The offset θ/2θ scan of the scattering vector in the layer normal direction (**Fig. S1**) suggests that the Si wafer and the SiC layer are both in their (0 0 1) crystal orientations. The diffraction peaks at 41.4° and 90.1° correspond to 3C-SiC (2 0 0) and 3C-SiC (4 0 0), respectively, whereas the peak at 69.2° corresponds to Si (4 0 0). The RSM in both symmetric and asymmetric geometries (**Fig. S2**) and the WR-RSM of the SiC/Si sample (Fig. 2**c**) clearly show that SiC and Si perfectly align along the (0 0 1) orientation with good crystallinity, which indicates the successful epitaxially growth of SiC on Si with minimum lattice distortion and interface defects. This may contribute to the efficient charge transfer between layers. This result is further supported by the selected area electron diffraction (SAED) measurement. The lattice fringes of SiC and Si can be seen clearly in the SAED pattern (**Fig. S3**), with the SAED pattern at the interface exhibiting a well-aligned orientation of the crystals of the two layers.

Next, the electronic characteristics of the SJ and DJ heterostructures are investigated. Fig. 2**d** depicts the current–voltage (I-V) curves of the heterostructures. The linearity of the graphs indicates that Ohmic contact between the Al electrodes and 3C-SiC was achieved. As seen in Fig. 2**d**, the current of the DJ structure is approximately 70 times greater than that of the SJ structure under dark conditions. We computed the resistivity of each structure to theoretically verify this difference. The doping concentration of the middle p-Si layer is 10^{16} atoms/cm^3, and the dopant is boron; thus, the resistivity of the middle p-Si layer is

approximately 0.197 Ohm·cm, while the resistivity of the p-3C-SiC layer is approximately 5 Ohm·cm [53]. This forms a p+/p junction between two layers p-3C-SiC and p-Si. Additionally, the resistances of all layers in the two devices were calculated as described in the Supporting Information. Because both the resistivity and resistance of the p-Si layer are lower than those of p-3C-SiC, the current in the DJ device is split into two paths, as shown in **Fig. S4**. A majority of charge carriers flow in the p-Si layer, and a small amount of charge carriers flow in the p-3C-SiC layer. This split current in p-Si layer is also partly due to the thin depletion layer (hence weak diode characteristics) of the heterojunction between these two p-3C-SiC and p-Si layers. For the SJ structure, the current flows primarily in the 3C-SiC layer because of the strong heterojunction diode property between p-3C-SiC and n-Si layers. This is due to the doping concentration of p-3C-SiC (5×10^{18} atoms/cm^3) is much higher than that of n-Si (10^{14} atoms/cm^3) and the different dopant types of the two layers.

3. 10,000 % boost in photocurrent and conversion power

3.1. LPC, LPV and conversion power of devices

The experimental setup to measure the lateral photovoltage (LPV) and lateral photocurrent (LPC) is shown in **Fig. S5**. A laser beam is focused on a position between the two electrodes on the surface of the p-3C-SiC layer. The LPV and LPC were measured across the two electrodes.

We initially set up a trio of laser diode-based light sources (637, 521, and 405 nm) and varied the laser power via current tuning. The power levels were measured by an external power meter. LPC and LPV measurements for both devices were taken when the laser was focused at a position 150 μm from the center position between the two electrodes. The results are shown in Fig. 3 and in **Table S2**. The LPC of the DJ device at λ = 637 nm is almost 100 times larger than that of the SJ device, while the LPV is nearly the same for both devices. The theoretical power (P_T) was computed from the short-circuit current (I_{SC}) and open-circuit voltage (V_{OC}), $P_T=V_{OC} \times I_{SC}$ (Table 1). It should be noted that the I_{SC} and V_{OC} are the LPC and LPV, respectively, without external resistors. Additionally, the maximum power $P_M=V_M \times I_M$ when the device was connected to an external resistor (V_M and I_M are the maximum values of LPV and LPC, respectively). The ratio of P_M to P_T was used as the fill factor (FF), and the results are provided in **Table S2**. According to the data in Table 1, the powers (P_M and P_T) of the DJ device are
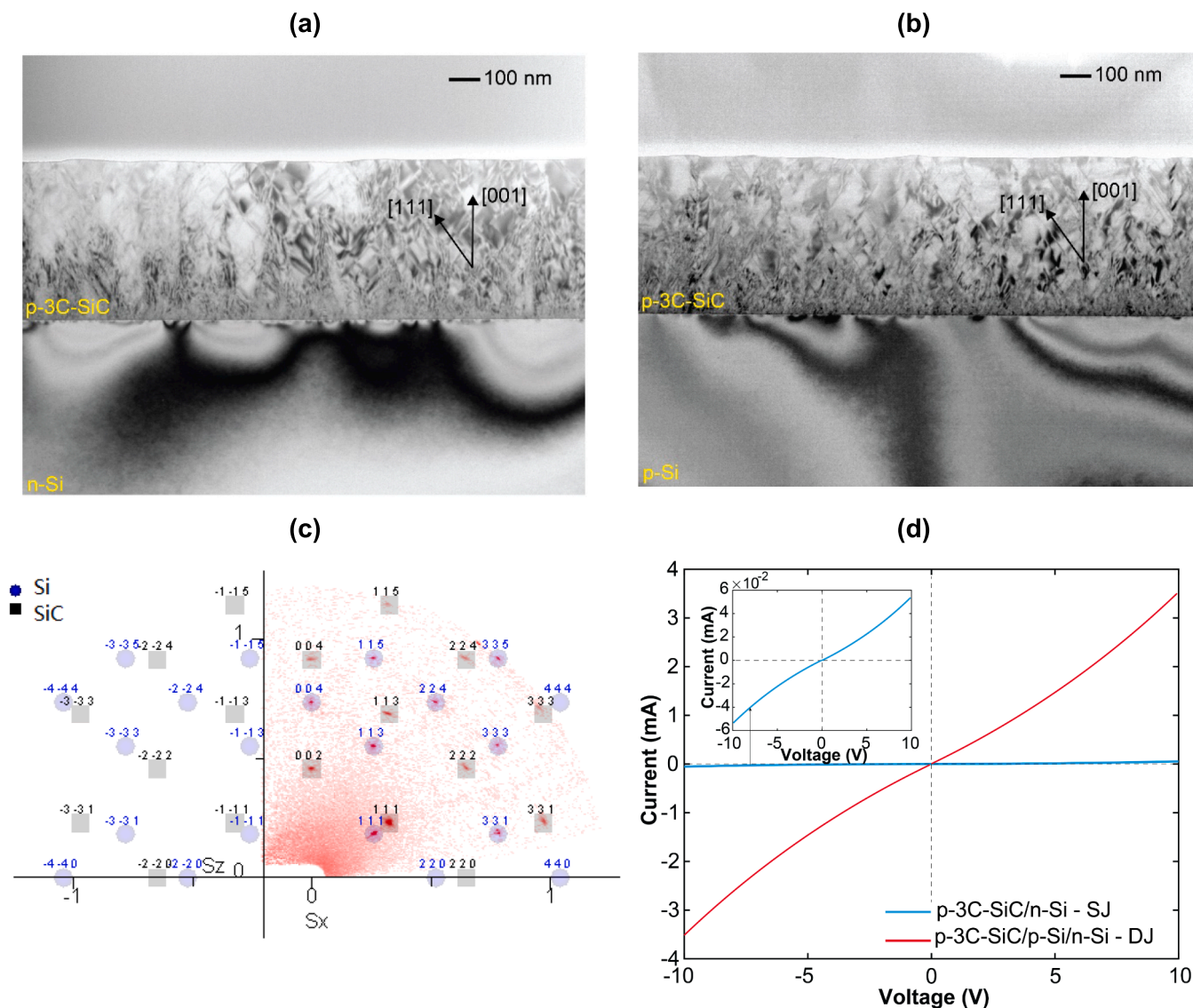
(a)

(b)

(c)

(d)

Fig. 2. Material crystal structure and electronic characterizations. (a) cross-sectional transmission electron microscopy (TEM) image of the SJ; (b) cross-sectional TEM image of the DJ; (c) Wide-range reciprocal space mapping (WR-RSM) of the 3C-SiC layer grown on p-Si/n-Si showing that the SiC (0 0 1) crystal orientation perfectly aligns with the Si (0 0 1) crystal orientation, with S=1/d (S is reciprocal vector and d is lattice spacing); (d) Current-voltage characteristics of the two structures under dark conditions.

approximately 100 times higher than those of the SJ device, showing that p-3C-SiC/p-Si/n-Si has a remarkable potential for harvesting photoenergy.

The photoresponses of both devices at three illumination powers (0.25, 1.0 and 3.0 mW) as the laser was periodically switched on and off as shown in Fig. 4. The laser was focused on a position 100 μm from the center position between the two electrodes. Fig. 4**a and b** illustrate the repeatability of the LPC, while that of the theoretical power (P_T) is shown in Fig. 4**c and d**. The LPC and P_T of both the DJ and SJ devices increase when the laser power increases, and the response and recovery times are approximately 0.22 s and 0.22 s, respectively. The measurement results demonstrate that the LPC, P_T, and P_M of the DJ structure are approximately 100 times greater than those of the SJ structure when the laser is focused at two positions, 100 μm and 150 μm from the center of the two electrodes. In other words, the efficiency of the DJ device is approximately 100 times greater than that of the SJ device at the same light input power. This demonstrates a massive conversion of light energy into electrical energy in a self-powered mode, highlighting the superior performance of the DJ device compared to that of the SJ device.

To the best of our knowledge, there has been no previous study that could achieve such a substantial energy conversion enhancement in a DJ heterostructure compared to its counterpart SJ heterostructure. It is expected that the results hold the potential to catalyse a significant breakthrough in the fields of sensing and energy harvesting.

3.2. Underpinned physics

To clearly explain the above results and understand the underpinning physics of this enhancement, the generation and transport mechanisms of charge carriers as well as the energy band diagrams need to be carefully analyzed. When two semiconductors of different types come into contact, a junction is formed between them [54]. In the p-3C-SiC/n-Si SJ structure, holes in the p-3C-SiC layer diffuse to the n-Si substrate, creating immobile negative ions at the junction. Meanwhile, electrons in the n-Si substrate diffuse into the p-3C-SiC layer, leaving positive ions at the junction. This process forms a depletion region across the junction, and a built-in electric field is generated across the junction of the heterostructure. This junction behaves as a diode. In the DJ structure, the
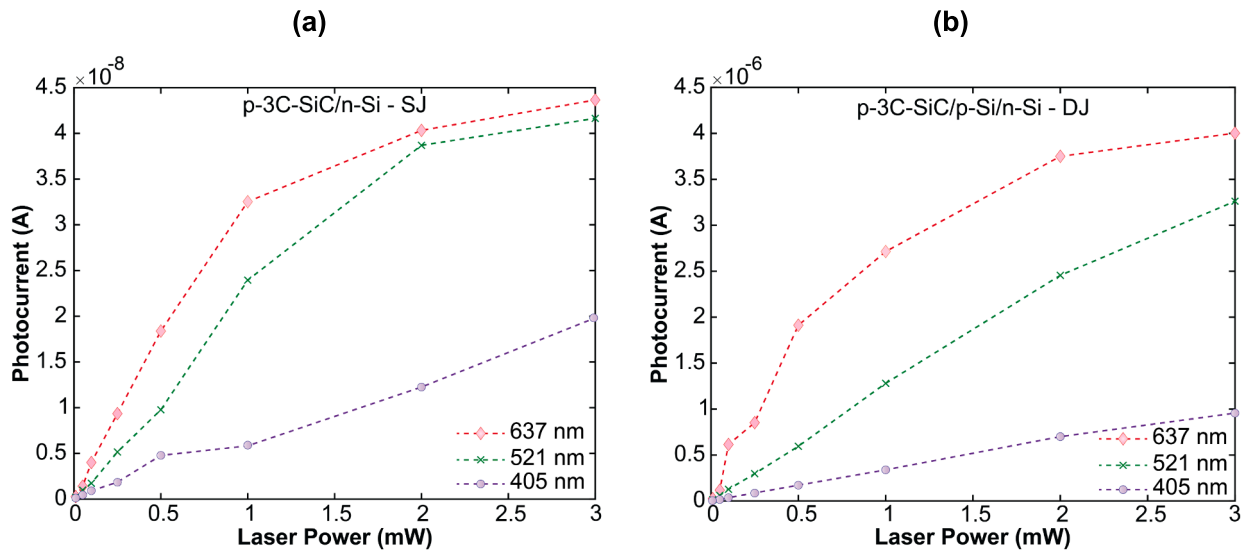
(a)

(b)

Fig. 3. LPC of the SJ device (a) and DJ device (b) at three wavelengths and various powers of the laser focused at 150 μm from the center position between the two electrodes.

Table 1
Theoretical and maximum powers of the SJ and DJ structures (wavelength λ = 637 nm, laser spot is at 150 μm from the center position between the two electrodes).

Laser Power (mW)	p-3C-SiC/n-Si − SJ		p-3C-SiC/p-Si/n-Si − DJ	
	P_T (W) = $V_{OC} \times I_{SC}$ $(\times 10^{-14})$	P_M (W) = $V_M \times I_M$ $(\times 10^{-14})$	P_T (W) = $V_{OC} \times I_{SC}$ $(\times 10^{-12})$	P_M (W) = $V_M \times I_M$ $(\times 10^{-12})$
0.01	9.65	7.53	8.13	7.16
0.05	239.73	196.58	207.31	180.36
0.1	1538.28	1281.39	1971.80	1794.34
0.25	9448.81	8333.85	7540.20	6710.71
0.5	35154.96	320964.80	32071.11	28415.01
1	104013.90	83211.12	88326.30	79493.68
2	199575.89	156667.07	206273.00	182551.75
3	216167.98	170772.71	225595.56	200780.06

junction formation is similar. However, the junction between the p-3C-SiC and p-Si layers is a junction of p + and p-type semiconductors and is created because of the different doping concentrations in these two layers. Since the p-3C-SiC layer is heavily doped at 5×10^{18} atoms/cm^3 while the middle p-Si layer's doping concentration is 10^{16} atoms/cm^3, holes diffuse from p-3C-SiC layer to the p-Si layer, creating negative charges at the junction. Similarly, the minority carrier electrons in p-Si move up to the p-3C-SiC layer, creating positively charged ions at the junction.

When the lasers irradiated the junctions, the electrons in the valence band were excited and tended to jump to the conduction band, leaving holes in the valence band. This process creates electron-hole (e-h) pairs near the illuminated area, which are separated at the junction due to the built-in electric field. The holes drift into the 3C-SiC layer, while the electrons move to the opposite direction, as shown in Fig. 5**a**. Furthermore, the holes also migrate from the n-Si layer up to the 3C-SiC layer via thermionic emission and tunnelling. In the DJ structure, e-h pairs are created at both junctions 1 (p-3C-SiC/p-Si) and 2 (p-Si/n-Si), and the holes move from the n-Si and p-Si layers toward the p-3C-SiC layer under the influence of two built in electric fields, as illustrated in Fig. 5**b**. Upon generation by photoexcitation, e-h pairs are separated by the built-in electric field of the junctions. Under a suitable wavelength (e.g. 637 nm in this paper), holes produced in the n-Si layer will migrate to the p-Si layer due to the built-in electric field of the p-Si/n-Si junction.

These holes will either be driven to the p-3C-SiC layer by the built-in voltage of p-3C-SiC/p-Si junction or diffuse laterally in the p-Si layer before reaching the p-3C-SiC layer at some point downstream. Therefore, with identical laser positioning, the hole concentration at the electrodes in the DJ structure will be significantly higher than that in the SJ structure. Consequently, the LPC measured in the DJ device is substantially greater than that in the SJ device.

The number of photogenerated e-h pairs depends on the wavelength of the laser. The red-coloured laser with a longer wavelength (637 nm) can penetrate deeper into the materials and generate more e-h pairs, resulting in higher LPV and LPC values (Fig. 3). The holes created in the p-3C-SiC/p-Si heterojunction drift into the p-3C-SiC layer, then diffuse in all directions, while the holes created in the p-Si/n-Si junction partially migrate to the p-3C-SiC layer and partially diffuse laterally in the p-Si layer. These holes then move up to the p-3C-SiC layer via thermionic, tunnelling and drift mechanisms. Since the mobility of holes in Si is much higher than that in 3C-SiC, the holes move faster in the p-Si layer, generating an enormous diffusion current. This results in a much larger LPC in the DJ device than in the SJ device. However, the experimental results revealed that the LPVs of the two structures are almost the same. This means that the differences in the charge carrier concentrations at the two electrodes on the SJ and DJ devices are the same, even though the charge carrier concentration in the DJ device is much higher (Fig. 5**c and d**). The LPV is proportional to the hole concentration gradient between the two electrodes. The charge carrier (hole) concentration at position x is described as follows [55]:

$$n(x) = n_0 \exp\left(-\frac{x}{l}\right) \tag{1}$$

where

$n(x)$: the charge carrier (hole) concentration at position x.
n_0: the charge carrier (hole) concentration at the illumination point.
x: the distance from the illumination point.
l: the diffusion length of the photoexcited charge carriers (holes).

The hole density is given by the theory of absorption as $n(\nu)$ (ν: the laser frequency) [56]:

$$n(\nu) = K(h\nu - E_g)^\alpha \tag{2}$$

where E_g is the energy bandgap of Si, K is a proportional coefficient, and α is an exponential coefficient.

Each electron among $n(\nu)$ can be statistically re-excited $\tau p/n(\nu)$ times on average (τ is a time-related coefficient, and p is the laser power) [57].
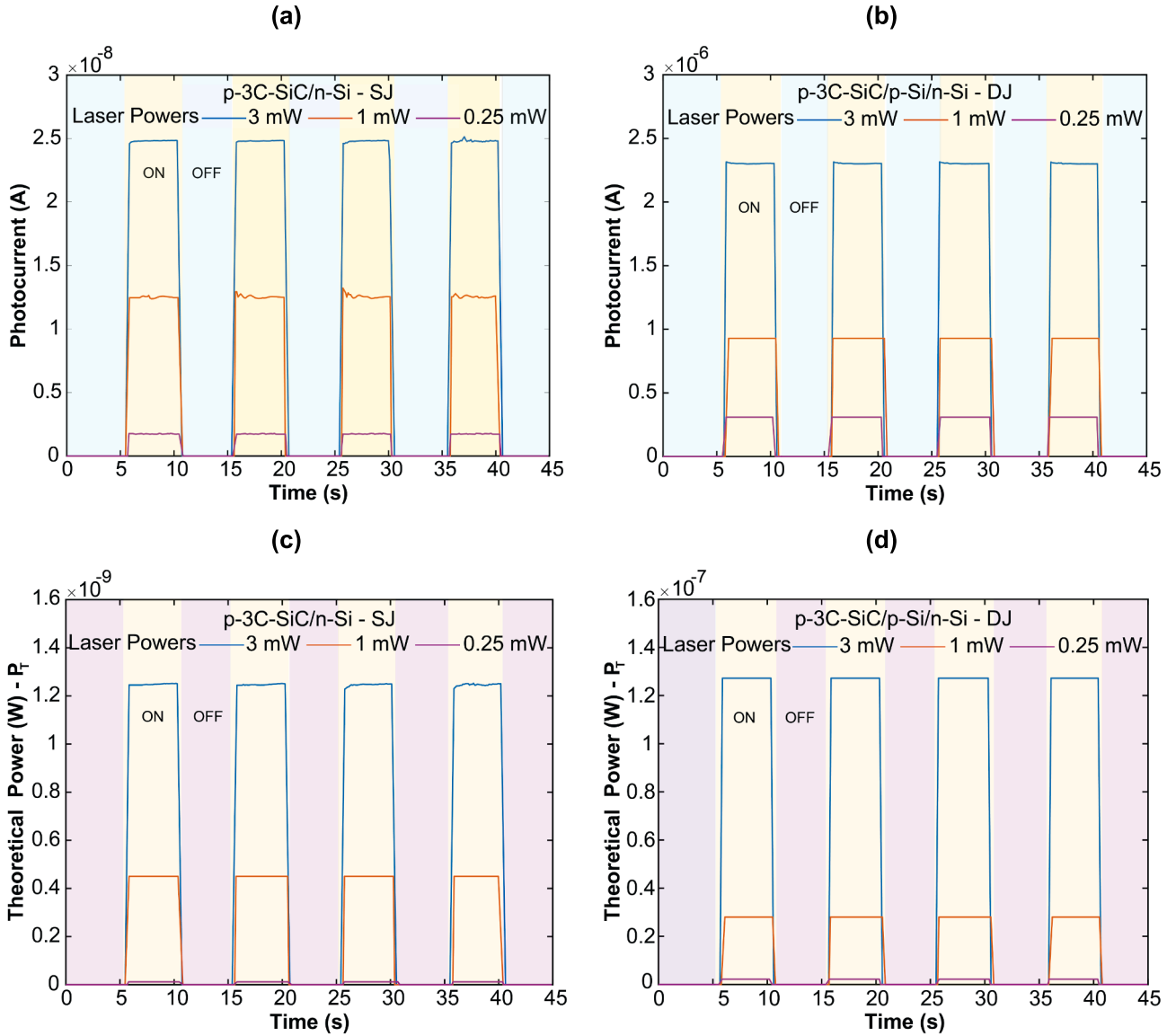
(a)

(b)

(c)

(d)

Fig. 4. Repeatability of the LPC and theoretical power under different illumination powers (wavelength $\lambda = 637$ nm; laser is focused at 100 μm away from the center between the two electrodes). (a) Repeatability of the LPC for the SJ structure; (b) repeatability of the LPC for the DJ structure; (c) repeatability of P_T for the SJ structure; (d) repeatability of P_T for the DJ structure.

The photogenerated e-h pairs are separated by the built-in electric field that sweeps the holes toward the 3C-SiC layer, whereas the electrons move toward the Si substrate. The injected hole concentration in 3C-SiC can be written as [57]:

$$N(\nu) = n(\nu)[1 - P_1^{(\tau p/n(\nu))}] \tag{3}$$

where P_1 is the probability that the holes recombine with electrons, and p is the laser power.

The LPV between two electrodes is calculated [58] as follows:

$$LPV = \frac{2C_2 N(\nu)}{l} \exp\left(-\frac{L}{l}\right) x \tag{4}$$

where C_2 is a proportional coefficient that depends on the Fermi levels, x is the laser position, and $2L$ is the distance between the two electrodes.

Additionally, the LPC linearly depends on the hole charge quantity (q) and the laser position (x) as follows [47,59,60]:

$$LPC = \frac{2qN(0)}{l^2} \exp\left(-\frac{L}{l}\right) x \tag{5}$$

where $N(0) = n_0 \times S$ (S is the cross-sectional area of the electrode).

As seen in Eq. (5), the magnitude of the LPC depends on the number of charge carriers (holes). Therefore, the enhanced LPC in the DJ heterostructure compared to the SJ heterostructure can now be elucidated by the substantially-increased generation of holes in the DJ structure.

To further explain the charge carrier transport mechanisms in the structures, energy band diagrams of the heterostructures are established and analysed. Energy bands of each material in the heterostructures were measured by using the ultraviolet photoelectron spectroscopy (UPS) as detailed in the **Method section**. To measure the energy bands of the middle p-Si layer in the DJ device, the top p-3C-SiC layer was removed. From the measured energy levels of each material, the energy band diagrams of the SJ and DJ heterostructures are established as shown in Fig. 6. The electrons move from E_c of SiC to E_c of Si easily because there is no barrier and $E_{c\_SiC} > E_{c\_Si}$. However, there is a barrier height of 1.06 eV between E_{v_Si} and E_{v_SiC}, so the holes move to SiC mainly by tunnelling, partly by thermionic emission mechanism.

For the SJ device, when the laser beam illuminates a position near electrode A, the hole concentration at electrode A is much higher than
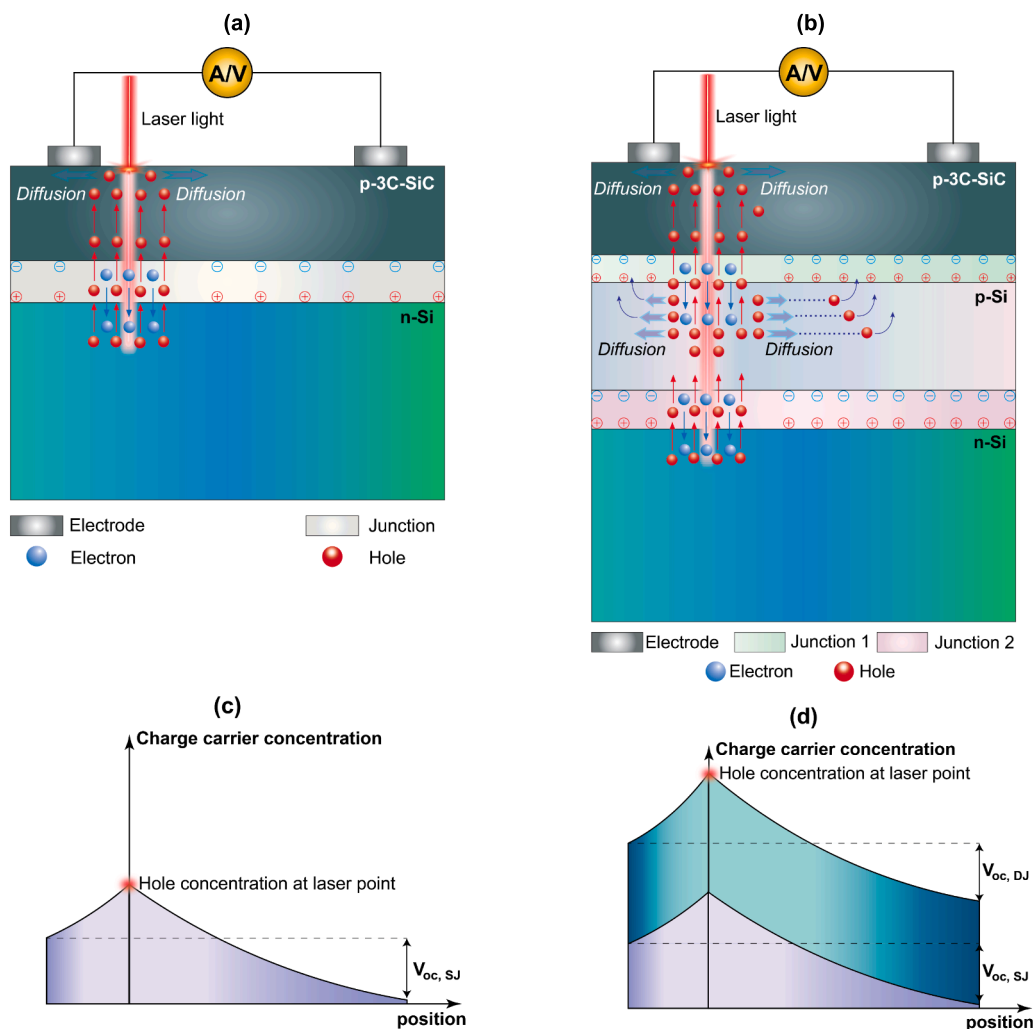
Fig. 5. Photogeneration and diffusion of charge carriers in the two heterostructures: (a) p-3C-SiC/n-Si SJ; (b) p-3C-SiC/p-Si/n-Si DJ; (c) charge carrier concentration distribution (purple) of the p-3C-SiC/n-Si under laser light; (d) charge carrier concentration distribution (green) of the p-3C-SiC/p-Si/n-Si under laser light. (For interpretation of the references to colour in this figure legend, the reader is referred to the web version of this article.)

that at electrode B, as the diffusion length of holes to electrode A is shorter, as shown in Fig. 6a. Therefore, the Fermi level of 3C-SiC at the electrode A moves closer to the valence band, while the Fermi level of 3C-SiC at the electrode B is almost unchanged (due to fewer holes diffuse to electrode B), resulting in a LPV between electrodes A and B because the potential energy at electrode A is lower than that at electrode B. The opposite results occur if the laser beam is focused on a position near electrode B. In addition, the LPC and LPV are zero when the laser position is at the center between the two electrodes.

For the DJ device, the working principle is the same as that for the SJ device. However, the number of charge carriers generated by the laser light in the DJ is much greater, and the generation and diffusion mechanisms have some differences. When laser light irradiates the DJ structure, electron-hole pairs are generated in n-Si, p-Si, p-3C-SiC and at the two junctions. The e-h pairs are split at the two junctions. More holes are injected into the p-Si and p-3C-SiC layers, as shown in Fig. 6b. In the p-Si layer, the holes laterally diffuse and move up to the p-3C-SiC layer through drift and tunnelling mechanisms. If the laser spot is near electrode A, then the hole concentration at electrode A is much higher than that at electrode B. During diffusion, there may be some recombination between electrons and holes. The difference between the numbers of charge carriers or the difference between the two Fermi levels at the two electrodes generates the LPV of the DJ device. Note that incident photons with long and visible wavelengths can be transmitted through the p-

3C-SiC layer and penetrate down to the n-Si layer, while more photons with short wavelengths are absorbed in the p-3C-SiC layer, and only a small portion reach the n-Si layer, resulting in more charge carriers being generated at visible and infrared wavelengths. Detailed explanations of the light penetration depth for each semiconductor layer in this study are provided in the Supporting Information. This explains why the LPC and LPV at longer wavelengths are higher than those generated by shorter wavelengths under the same laser power.

The physic phenomena including efficient photogeneration of charge carriers, electron-hole pair splitting, energy bands and the charge carrier transport mechanisms in the heterojunctions have been explained comprehensively, facilitating an understanding of the movement of the charge carriers and the underlying reasons for significant energy conversion efficiency in the DJ device.

4. Ultrahigh sensitive position detectors

This section demonstrates the advantage of the DJ structure over the SJ structure in position sensitive detector (PSD) applications. Fig. 7 shows the position-sensitive characteristics of the SJ and DJ devices. Fig. 7a and b show the linear relationships between the laser position and LPC for three different wavelengths at 2 mW laser power. This relationship agrees well with Equation (5), which defines the LPC as a linear function of the laser position.
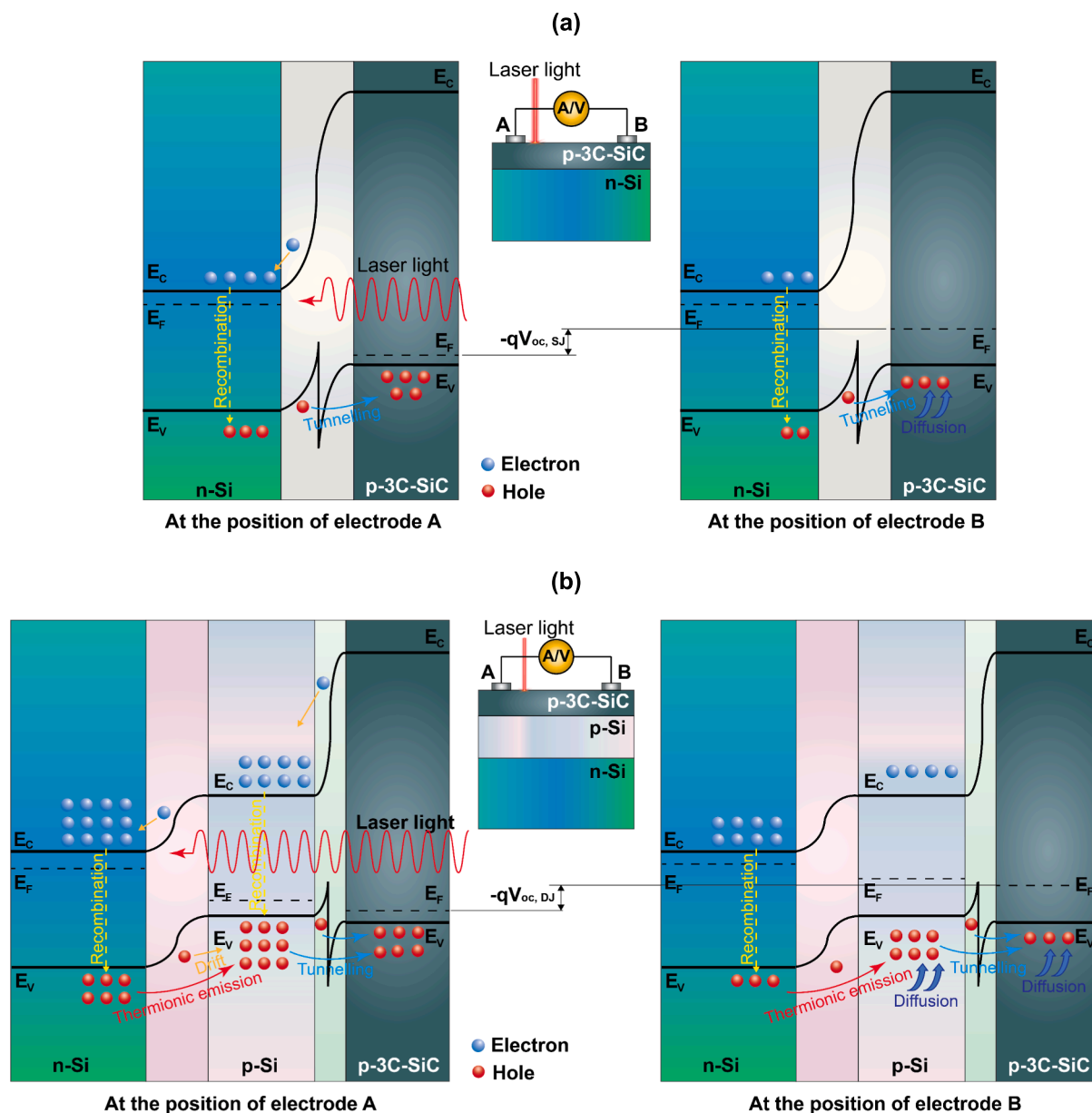
(a)

(b)

Fig. 6. Energy band diagram and charge carrier transport mechanism. (a) Energy band diagrams of the SJ device when the laser spot is near electrode A; (b) energy band diagrams of the DJ device when the laser spot is near electrode A.

When the laser is focused at the center point between the two electrodes, the LPC becomes zero because an equal number of holes move toward each electrode; hence, there is no hole concentration gradient between the two electrodes. Additionally, the LPC increases when the laser spot moves toward an electrode. As shown in Fig. 7c and d, the best sensitivities of the SJ and DJ devices are 2.6×10^{-7} A/mm and 2.6×10^{-5} A/mm, respectively, at a laser power of 3 mW and a wavelength of 637 nm. As can be seen, the sensitivity of the DJ structure is 100 times higher than that of the SJ structure. The performance parameters of SJ and DJ-based on PSDs describes through Table S3. The physics underpinning this phenomenon are explained above. At shorter wavelengths, the sensitivity of the DJ structure is 50–80 times higher than that of the SJ heterostructure. This shows the superior response and performance of the DJ structure, especially in the long and visible wavelength ranges. In comparison to the SJ device with the same production cost, the DJ device demonstrates an enormous potential in energy harvesting and optoelectronic sensing applications.

5. Conclusion

This paper reports the superiority in energy conversion and LPC of a p-3C-SiC/p-Si/n-Si DJ structure compared to a p-3C-SiC/n-Si SJ structure under the same conditions. The fabrication of wafers and devices is demonstrated to be flawless based on the evidence provided by XRD, RSM, WR-RSM, TEM, and I-V characteristics measurements. Importantly, this study demonstrated that the introduction of a middle p-Si layer with a higher hole mobility than the top 3C-SiC layer to form the DJ structure has resulted in more charge carriers generated, a stronger electron-hole pair separating at the junctions, a slower recombination rate, and a significant lateral hole diffusion in the middle p-Si layer. This, in turn, leads to substantial increases in the LPC and maximum power, showcasing the importance of this layer in enhancing the overall performance of the DJ structure. An explanation for this phenomenon was proposed based on the generation and transport mechanisms of charge carriers, as well as the energy band diagrams. In addition, the DJ heterojunction, when used as a PSD, achieved the best sensitivity of
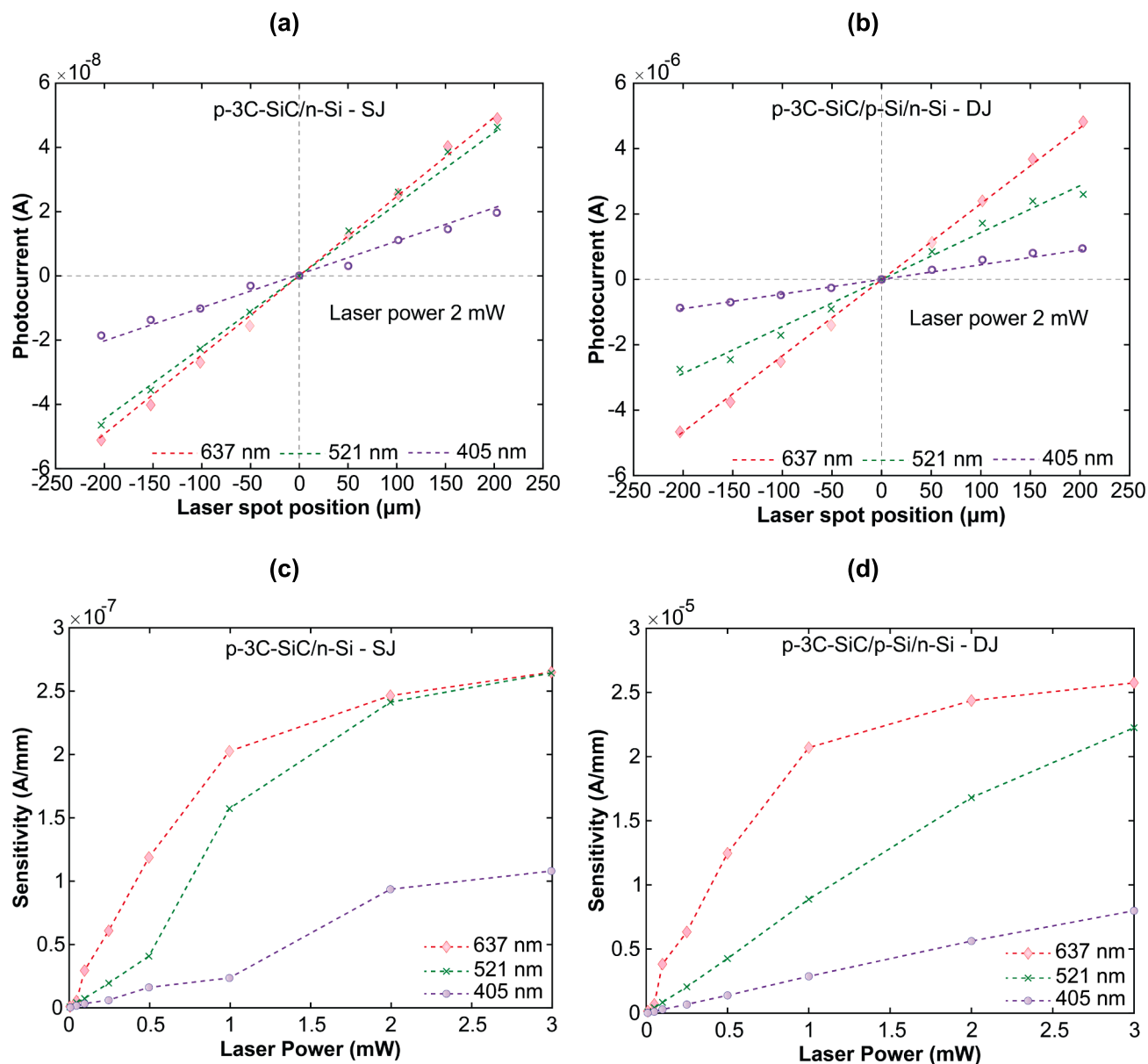
(a)

(b)

(c)

(d)

Fig. 7. Characteristics of the position detector. Position-dependent LPC of the SJ device (a) and the DJ device (b) when the laser beam scans between the two electrodes with an electrode spacing of 500 μm; lateral sensitivity of the SJ device (c) and the DJ device (d) under laser illumination at 637 nm, 521 nm and 405 nm.

2.6×10^{-5} A/mm at a laser power of 3 mW and a wavelength of 637 nm, which is almost 100 times more sensitive than the SJ PSD under the same conditions. This research marks a significant milestone for the development of optoelectronic sensing devices with high sensitivity and substantial power conversion capabilities.

6. Methods

6.1. Fabrication of the p-3C-SiC/p-Si/n-Si and p-3C-SiC/n-Si wafers

The fabrication of the wafers was performed by the Japan-based company D&X (detailed in the Supporting Information). The 500 nm 3C-SiC (1 0 0) epilayer was grown on a Si wafer in a single-wafer cold-wall chemical vapor deposition (CVD) reactor at a temperature of approximately 1100 °C. The p-type dopants were introduced into the epilayers during epitaxial growth, and the dopant concentration was controlled via calibration on the basis of secondary ion mass spectrometry (SIMS) and resistivity measurements. The middle p-Si layer

was grown using the same CVD method used for the p-3C-SiC top layer. The carrier concentrations of the grown p-3C-SiC film and the n-Si substrate were approximately 5×10^{18} and 10^{14} atoms/cm^3, respectively, while that of the middle p-type Si layer was 10^{16} atoms/cm^3. The thicknesses of the p-3C-SiC and n-Si layers of both structures were 500 nm and approximately 500 μm, respectively. The thickness of the middle p-Si layer was 1 μm. The dopant of the p-type 3C-SiC layer and the middle p-type Si layer was boron, while the n-type Si substrate was doped with phosphorus (detailed in Supporting Information).

6.2. Fabrication process of the heterostructures

The steps involved in the device fabrication process are illustrated in Fig. 8 with Steps 1 to 3 caried out by the D&X Company. The fabrication of the SJ device was similar, except that p-3C-SiC was directly grown on the n-Si substrate. A standard process for fabricating 3C-SiC/Si devices was applied, and all the samples were fabricated in a cleanroom at the ***Queensland Micro and Nanotechnology Centre, Griffith University.***
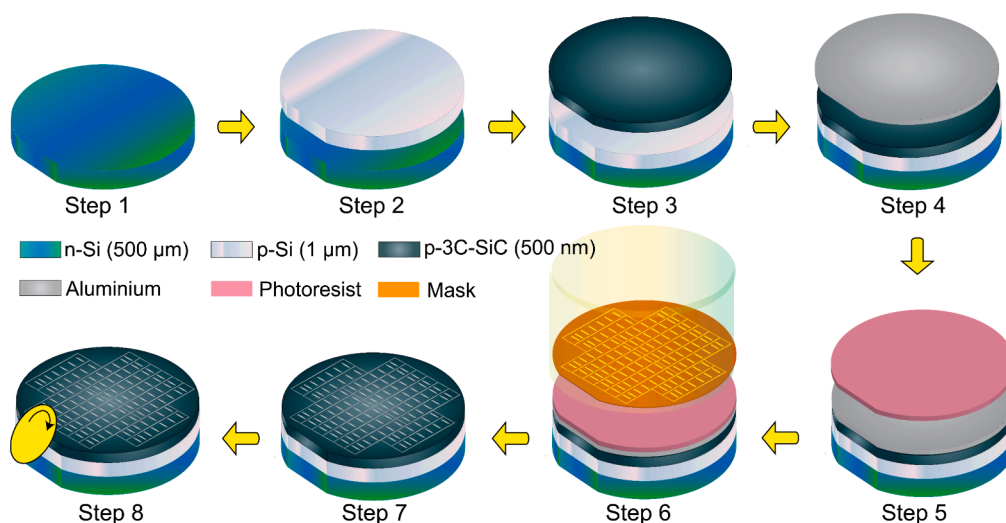
Fig. 8. Fabrication of the DJ device. Note that Steps 1 to 3 were conducted by D&X Co., Ltd. Step 1: preparation of the n-Si wafer; Step 2: growth of p-Si on the n-Si substrate by low-pressure chemical vapor deposition (LPCVD); Step 3: growth of p-3C-SiC on p-Si/n-Si by LPCVD; Step 4: deposition of aluminum (Al) on the p-3C-SiC thin film; Step 5: spin coating of a photoresist layer; Step 6: photolithography to define electrode patterns; Step 7: wet etching of deposited Al and removal of the photoresist layer; Step 8: dicing of the samples from the wafer.

Before sputtering the Al layer on the surface of the 3C-SiC film, the samples were cleaned with 4:1 piranha solution (a mixture of sulfuric acid – H_2SO_4 – and hydrogen peroxide – H_2O_2) for approximately 15 min and then immersed in HF (1 %) for 1 min to remove the residues and oxide on the surface. A photoresist layer (AZ 1512) was coated on the Al layer by spin-coating at 3500 rpm. Photolithography was conducted to pattern the electrodes, and wet etching was carried out to form the Al electrodes. It should be noted that the wavelength and exposure time used for photolithography are 405 nm and 30 min, respectively while the materials used in wet etching is H_3PO_4: CH_3COOH: $HNO_3 = 20:4:1$. Finally, the samples were diced from the wafers.

After dicing of the devices, annealing [39] was carried out to ensure ohmic contact between the Al electrodes and the p-3C-SiC thin film. Annealing was performed in dry nitrogen (N_2) at 600 °C for 4 min to form Al-3C-SiC alloy junctions.

6.3. Material characterization

6.3.1. Crystal structure characterization
Reciprocal space mapping (RSM) and wide range reciprocal space mapping (WR-RSM)

The epitaxial SiC layer on the Si substrate was precisely aligned on an RxRy attachment head on the φ stage of a Rigaku SmartLab diffractometer with CuKα1 radiation (λ = 1.54 Å) operated at 40 kV, 40 mA. A CBO parallel beam mirror followed by a Ge(220x2) two-bounce monochromator were used on the primary side. A motorized antiscattering slit, i.e., a 5° axial Soller slit, was used before a Hypix3000 detector in 0D mode. Offset θ/2 θ scans in both the Si ⟨0 0 1⟩ direction and the Si ⟨3 1 1⟩ direction were conducted to explore the crystal orientation relationship between the SiC layer and the Si template. In this case, scans in symmetric direction ⟨0 0 1⟩ and asymmetric direction ⟨3 1 1⟩ are required to confirm the aligned relationship between two layers. RSMs for Si/SiC⟨0 0 4⟩, Si/SiC $<3\overline{1}1>$, and Si/SiC⟨5 1 1⟩ spots were successfully recorded.

WR-RSM for the whole measurable reciprocal space was conducted to verify the relationship between the SiC layer and the Si substrate. The sample was aligned on a χ-φ cradle. A primary point focus beam was achieved by a CBO-PB0.5 mm pinhole, a CBO-f poly-capillary module and a long collimator with a diameter of 0.8 mm. A Hypix3000 detector was placed 121 mm from the sample and recorded 2D diffraction frames for "Chi-expansion" merging via Rigaku 2PD software, and the final WR-

RSM plot was generated by means of Rigaku 3D Explore software.

6.3.2. Energy band characterization
Ultraviolet photoelectron spectroscopy (UPS) measurement

A Kratos AXIS Supra photoelectron spectrometer (HeI radiation, hν = 21.22 eV) was used to measure UPS energy state of the material. Prior to UPS measurement, the samples were cleaned and etched by argon ion sputter (for p-Si measurement of the DJ device). Specifically, the UPS spectra of the material show the kinetic energy of photoelectrons emitted as a result of the photoelectric effect in Fig. 9. The valence band energy (E_v) was calculated on the basis of the energy of the incident photons (HeI: 21.22 eV) and the onset of the emitted electron intensity determined from the spectra.

The energy bands of each semiconductor determined by analysing the UPS spectra are shown in Fig. 10**a and b**, and the energy band diagrams of the two devices under dark conditions are shown in Fig. 10**c and d**. The Fermi levels of 3C-SiC ($E_{F-3C-SiC}$) at the two electrodes are aligned under dark conditions at thermal equilibrium in both devices. Both the LPV and LPC are zero in this case.

CRediT authorship contribution statement

Dinh Gia Ninh: Conceptualization, Fabrication, Investigation, Methodology, Formal analysis, Data curation, Validation, Writing – original draft, Writing – review & editing. **Minh Tam Hoang:** Writing – original draft, Investigation, Formal analysis, Data curation. **Tony Wang:** Writing – original draft, Formal analysis. **Tuan-Hung Nguyen:** Writing – review & editing, Investigation, Formal analysis, Data curation. **Tuan-Khoa Nguyen:** Writing – review & editing, Formal analysis. **Erik Streed:** Writing – review & editing, Resources, Formal analysis. **Hongxia Wang:** Writing – review & editing, Supervision, Resources. **Yong Zhu:** Writing – review & editing, Supervision. **Nam-Trung Nguyen:** Writing – review & editing, Supervision, Resources. **Van Dau:** Writing – review & editing, Formal analysis. **Dzung Viet Dao:** Writing – review & editing, Supervision, Project administration, Methodology, Investigation, Conceptualization.

Declaration of competing interest

The authors declare that they have no known competing financial interests or personal relationships that could have appeared to influence
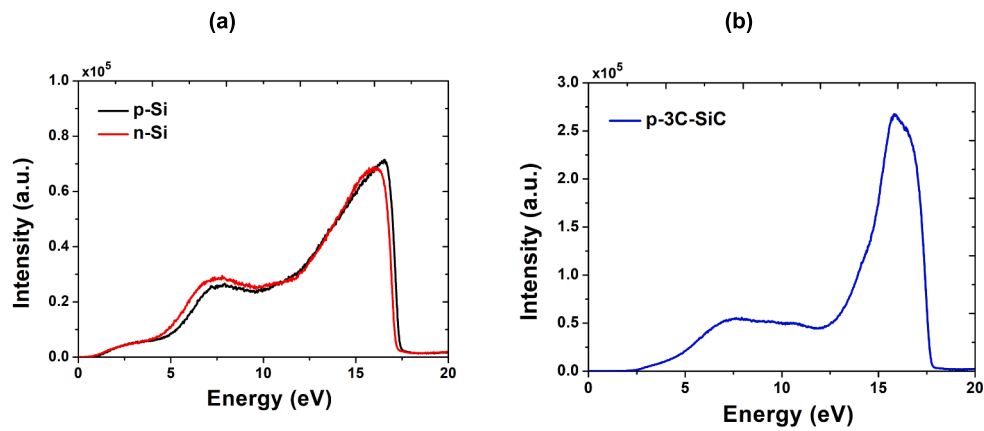
Fig. 9. **UPS spectra of each semiconductor layer in the SJ and DJ structures.** (a) n-Si (SJ and DJ) and p-Si (DJ); (b) p-3C-SiC (SJ and DJ).
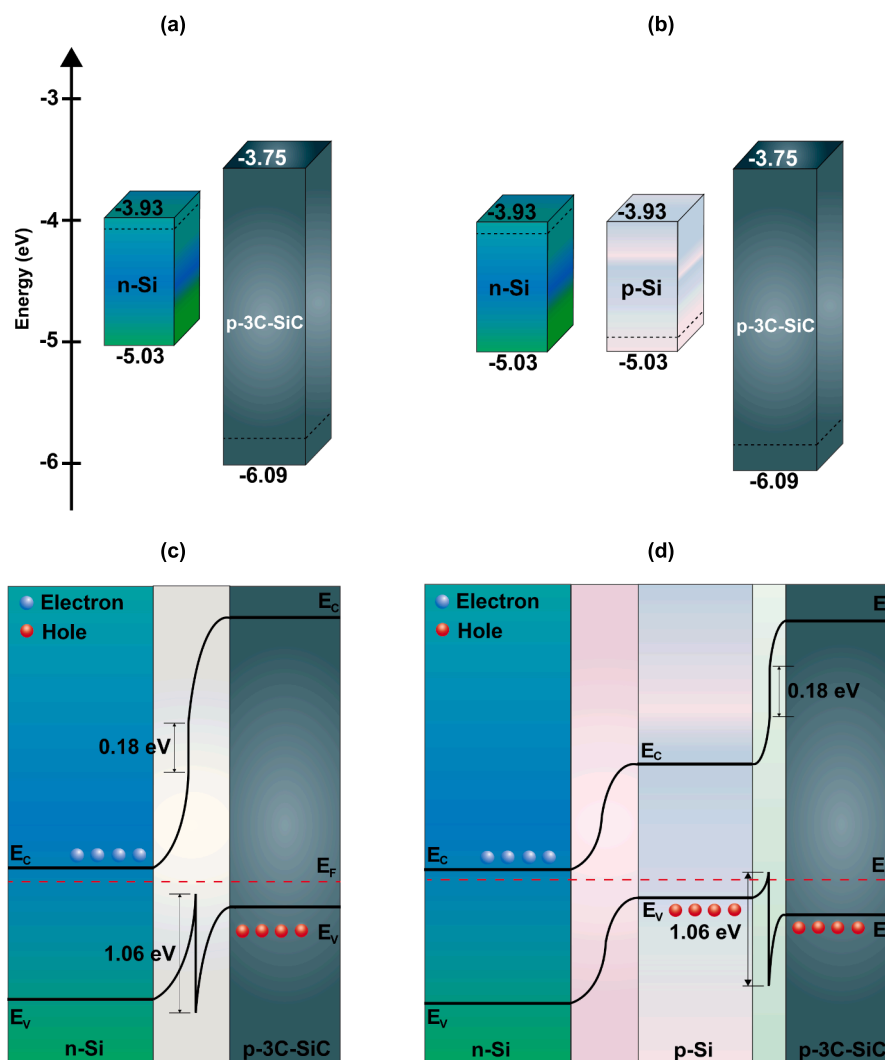

Fig. 10. Energy band diagrams of each semiconductor in the SJ structure (a) and the DJ structure (b) were determined from UPS measurements. Energy band diagrams of the SJ structure (c) and the DJ structure (d).

the work reported in this paper.

Acknowledgements

of Queensland. The measurement of the UPS intensity for determining energy band of semiconductor layers and the XRD measurement were supported by Central Analytical Research Facility (CARF), Queensland University of Technology. The authors are grateful for the support of research centers and funds.

Appendix A. Supplementary data

Supplementary data to this article can be found online at https://doi.org/10.1016/j.cej.2024.153774.

References

[1] A.I. Osman, L. Chen, M. Yang, G. Msigwa, M. Farghali, S. Fawzy, P.S. Yap, Cost, environmental impact, and resilience of renewable energy under a changing climate: a review, Environ. Chem. Lett. 21 (2) (2023) 741–764.

[2] T. Das, P. Biswas, A. Dev, J. Mallick, M. Kar, Multi-functional piezoelectric nanogenerator based on relaxor ferroelectric materials (BSTO) and conductive fillers (MWCNTs) for self-powered memristor and optoelectronic devices, Chem. Eng. J. 479 (2024) 147900.

[3] S. Tan, T. Huang, I. Yavuz, R. Wang, T.W. Yoon, M. Xu, Y. Yang, Stability-limiting heterointerfaces of perovskite photovoltaics, Nature 605 (7909) (2022) 268–273.

[4] K.T. Huang, C.C. Chueh, W.C. Chen, Recent advance in renewable materials and green processes for optoelectronic applications, Materials Today Sustainability 11 (2021) 100057.

[5] J. Sun, Y. Liu, J. Wei, P. Wei, T. Chen, Pseudo-photoelectric cascade conversion endowing photosensitive Janus ionogel for solar energy harvesting and sensing, Chem. Eng. J. (2024) 149836.

[6] C.T. Nguyen, D. Gia Ninh, T.H. Nguyen, T.H. Vu, D.D.H. Tran, B. Tong, D.V. Dao, Vertical piezo-optoelectronic coupling in a 3C-SiC/Si heterostructure for self-powered and highly sensitive mechanical sensing, ACS Appl. Mater. Interfaces 15 (23) (2023) 28781–28789.

[7] H. Jinno, S.B. Shivarudraiah, R. Asbjörn, G. Vagli, T. Marcato, F.T. Eickemeyer, C. J. Shih, Indoor Self-Powered Perovskite Optoelectronics with Ultraflexible Monochromatic Light Source, Adv. Mater. (2023) 2304604.

[8] Q. Mahmood, M. Hassan, S.H.A. Ahmad, A. Shahid, A. Laref, Study of optoelectronic and thermoelectric properties of BaSiO3 perovskite under moderate pressure for energy renewable devices applications, J. Phys. Chem. Solid 120 (2018) 87–95.

[9] P. Zhu, D. Wang, Y. Zhang, Z. Liang, J. Li, J. Zeng, B. Xu, Aqueous synthesis of perovskite precursors for highly efficient perovskite solar cells, Science 383 (6682) (2024) 524–531.

[10] W.M. Gu, K.J. Jiang, X. Jiao, L. Wu, C.Y. Gao, X.H. Fan, Y. Song, Poly (3, 4-Ethylenedioxythiophene) as a Hole-Transport layer for highly efficient and stable inverted perovskite solar cells, Chem. Eng. J. (2024) 149512.

[11] T. Tan, X. Jiang, C. Wang, B. Yao, H. Zhang, 2D material optoelectronics for information functional device applications: status and challenges, Adv. Sci. 7 (11) (2020) 2000058.

[12] W. Zhang, T. Zhang, L. Qin, S.Z. Kang, Y. Zhao, X. Li, Anti-solvent engineering to rapid purify PbI2 for efficient perovskite solar cells, Chem. Eng. J. 479 (2024) 147838.

[13] Y. Kim, Y. Yang, X. Zhang, Z. Li, A. Vázquez-Guardado, I. Park, R. Bashir, Remote control of muscle-driven miniature robots with battery-free wireless optoelectronics, Sci. Rob. 8 (74) (2023) eadd1053.

[14] O. Sergiyenko, (Ed.)., Optoelectronic Devices in Robotic Systems, Springer Nature, 2022.

[15] A. Hagfeldt, S.E. Lindquist, M. Grätzel, Charge carrier separation and charge transport in nanocrystalline junctions, Sol. Energy Mater. Sol. Cells 32 (3) (1994) 245–257.

[16] H.S. Kim, M.D. Kumar, M. Patel, J. Kim, B. Cho, D.H. Kim, High-performing MoS2-embedded Si photodetector, Mater. Sci. Semicond. Process. 71 (2017) 35–41.

[17] R.A. Ismail, A.M.E. Al-Samarai, A.Y. Ali, Preparation and characteristics study of CdS/macroporous silicon/c-Si double heterojunction photodetector by spray pyrolysis technique, Optik 168 (2018) 302–312.

[18] Z. Luo, M. Yang, D. Wu, Z. Huang, W. Gao, M. Zhang, J. Li, Rational Design of WSe2/WS2/WSe2 Dual Junction Phototransistor Incorporating High Responsivity and Detectivity, Small Methods 6 (9) (2022) 2200583.

[19] S. Bansal, A. Das, P. Jain, K. Prakash, K. Sharma, N. Kumar, A.K. Singh, Enhanced optoelectronic properties of bilayer graphene/HgCdTe-based single-and dual-junction photodetectors in long infrared regime, IEEE Trans. Nanotechnol. 18 (2019) 781–789.

[20] S. Bansal, K. Prakash, K. Sharma, N. Sardana, S. Kumar, N. Gupta, A.K. Singh, A highly efficient bilayer graphene/ZnO/silicon nanowire based heterojunction photodetector with broadband spectral response, Nanotechnology 31 (40) (2020) 405205.

[21] Y. Kim, K. Kim, T.W. Kim, L.J. Mawst, T.F. Kuech, C.Z. Kim, J. Lee, InGaAsNSb/Ge double-junction solar cells grown by metalorganic chemical vapor deposition, Sol. Energy 102 (2014) 126–130.

[22] J. Fang, Q. Ren, F. Wang, C. Wei, B. Yan, Y. Zhao, X. Zhang, Amorphous silicon/crystal silicon heterojunction double-junction tandem solar cell with open-circuit voltage above 1.5 V and high short-circuit current density, Sol. Energy Mater. Sol. Cells 185 (2018) 307–311.

[23] M.R. Lueck, C.L. Andre, A.J. Pitera, M.L. Lee, E.A. Fitzgerald, S.A. Ringel, Dual junction GaInP/GaAs solar cells grown on metamorphic SiGe/Si substrates with high open circuit voltage, IEEE Electron Device Lett. 27 (3) (2006) 142–144.

[24] R. Gottschalg, T.R. Betts, D.G. Infield, M.J. Kearney, The effect of spectral variations on the performance parameters of single and double junction amorphous silicon solar cells, Sol. Energy Mater. Sol. Cells 85 (3) (2005) 415–428.

[25] S. Essig, C. Allebé, T. Remo, J.F. Geisz, M.A. Steiner, K. Horowitz, A. Tamboli, Raising the one-sun conversion efficiency of III–V/Si solar cells to 32.8% for two junctions and 35.9% for three junctions, Nat. Energy 2 (9) (2017) 1–9.

[26] A. Kuddus, A.B.M. Ismail, J. Hossain, Design of a highly efficient CdTe-based dual-heterojunction solar cell with 44% predicted efficiency, Sol. Energy 221 (2021) 488–501.

[27] W. Fu, A.G. Ricciardulli, Q.A. Akkerman, R.A. John, M.M. Tavakoli, S. Essig, M. Saliba, Stability of perovskite materials and devices, Mater. Today 58 (2022) 275–296.

[28] G.E. Eperon, T. Leijtens, K.A. Bush, R. Prasanna, T. Green, J.T.W. Wang, H. J. Snaith, Perovskite-perovskite tandem photovoltaics with optimized band gaps, Science 354 (6314) (2016) 861–865.

[29] J. Zhu, J. Xiu, J. Zheng, X. Li, H. Luo, Y. Li, M. Wei, Fine optimized cation immobilization strategy for enhancing stability and efficiency of perovskite solar cells, Chem. Eng. J. 150382 (2024).

[30] G.M. Mustafa, N.A. Noor, M.W. Iqbal, M. Sajjad, M.A. Naeem, Q. Mahmood, W. Al-Masry, Study of optoelectronic and transport properties of MgLu2Z4 (Z= S, Se) spinels for optoelectronic and energy harvesting applications, Mater. Sci. Semicond. Process. 121 (2021) 105452.

[31] S. Lin, Y. Lu, J. Xu, S. Feng, J. Li, High performance graphene/semiconductor van der Waals heterostructure optoelectronic devices, Nano Energy 40 (2017) 122–148.

[32] Q. Zhou, J.G. Park, K.N. Kim, A.K. Thokchom, J. Bae, J.M. Baik, T. Kim, Transparent-flexible-multimodal triboelectric nanogenerators for mechanical energy harvesting and self-powered sensor applications, Nano Energy 48 (2018) 471–480.

[33] X. Wang, Y. Cui, T. Li, M. Lei, J. Li, Z. Wei, Recent advances in the functional 2D photonic and optoelectronic devices, Adv. Opt. Mater. 7 (3) (2019) 1801274.

[34] H. Kim, Y.C. Kim, Y.H. Ahn, Y. Yoo, In-plane mixed-dimensional 2D/2D/1D MoS2/ MoTe2/Mo6Te6 heterostructures for low contact resistance optoelectronics, Chem. Eng. J. 468 (2023) 143678.

[35] X. Du, Y. Li, Z. Yu, C.M. Oh, Y. Zhang, F. Liu, S.H. Park, Multi-functional ion-pairing additive for efficient quasi-2D perovskite light-emitting diodes and solar cells, Chem. Eng. J. (2024) 150596.

[36] Z. Luo, H. Xu, W. Gao, M. Yang, Y. He, Z. Huang, J. Li, High-Performance and Polarization-Sensitive Imaging Photodetector Based on WS2/Te Tunneling Heterostructure, Small 19 (15) (2023) 2207615.

[37] M. Mehregany, C.A. Zorman, N. Rajan, C.H. Wu, Silicon carbide MEMS for harsh environments, Proc. IEEE 86 (8) (1998) 1594–1609.

[38] D.G. Senesky, B. Jamshidi, K.B. Cheng, A.P. Pisano, Harsh environment silicon carbide sensors for health and performance monitoring of aerospace systems: A review, IEEE Sens. J. 9 (11) (2009) 1472–1478.

[39] P. Tanner, A. Iacopi, H.P. Phan, S. Dimitrijev, L. Hold, K. Chaik, N.T. Nguyen, Excellent rectifying properties of the n-3C-SiC/p-Si heterojunction subjected to high temperature annealing for electronics, MEMS, and LED applications, Sci. Rep. 7 (1) (2017) 17734.

[40] T.K. Nguyen, H.P. Phan, T. Dinh, T. Toriyama, K. Nakamura, A.R.M. Foisal, D. V. Dao, Isotropic piezoresistance of p-type 4H-SiC in (0001) plane, Appl. Phys. Lett. 113 (1) (2018).

[41] T. Toriyama, Piezoresistance consideration on n-type 6H SiC for MEMS-based piezoresistance sensors, J. Micromech. Microeng. 14 (11) (2004) 1445.

[42] H.P. Phan, D.V. Dao, K. Nakamura, S. Dimitrijev, N.T. Nguyen, The piezoresistive effect of SiC for MEMS sensors at high temperatures: a review, J. Microelectromech. Syst. 24 (6) (2015) 1663–1677.

[43] W. Jatal, U. Baumann, K. Tonisch, F. Schwierz, J. Pezoldt, High-frequency performance of GaN high-electron mobility transistors on 3C-SiC/Si substrates with Au-free ohmic contacts, IEEE Electron Device Lett. 36 (2) (2014) 123–125.

[44] D. Dochev, V. Desmaris, A. Pavolotsky, D. Meledin, Z. Lai, A. Henry, V. Belitsky, Growth and characterization of epitaxial ultra-thin NbN films on 3C-SiC/Si substrate for terahertz applications, Supercond. Sci. Technol. 24 (3) (2011) 035016.

[45] C.M. Lin, Y.Y. Chen, V.V. Felmetsger, W.C. Lien, T. Riekkinen, D.G. Senesky, A. P. Pisano, Surface acoustic wave devices on AlN/3C–SiC/Si multilayer structures, J. Micromech. Microeng. 23 (2) (2013) 025019.

[46] R. Kagawa, K. Kawamura, Y. Sakaida, S. Ouchi, H. Uratani, Y. Shimizu, N. Shigekawa, AlGaN/GaN/3C-SiC on diamond HEMTs with thick nitride layers prepared by bonding-first process, Appl. Phys. Express 15 (4) (2022) 041003.

[47] C. Hu, X. Wang, B. Song, High-performance position-sensitive detector based on the lateral photoelectrical effect of two-dimensional materials, Light Sci. Appl. 9 (1) (2020) 88.

[48] Z. Huang, M. Yang, Z. Qiu, Z. Luo, Y. Chen, C. Du, J. Li, Mixed-dimensional WS2/ WSe2/Si unipolar barrier heterostructure for high-performance photodetection, Sci. China Mater. 66 (6) (2023) 2354–2363.

[49] Q. Zheng, Z. Qiu, Q. Zhang, M. Yang, J. Lei, L. Han, J. Li, ReS2 nanosheet/WS2 nanosheet/p-GaN substrate dual junction photodetectors, ACS Appl. Nano Mater. 6 (17) (2023) 15490–15497.

[50] M. Javadi, M. Gholami, Y. Abdi, IR position-sensitive detectors based on double-junction asymmetric TiO 2/MoS 2/reduced graphene-oxide sandwiches, J. Mater. Chem. C 6 (31) (2018) 8444–8452.

[51] S. Liu, A. Dong, X. Dong, Y. Niu, D. Zheng, H. Wang, Heterojunction interface-induced enhancement of position-sensitive photodetection in the nano-film of Ti/SrTiO 3 based on the p-type silicon, Opt. Lett. 46 (13) (2021) 3041–3044.

[52] S. Qiao, B. Zhang, K. Feng, R. Cong, W. Yu, G. Fu, S. Wang, Large lateral photovoltage observed in MoS2 thickness-modulated ITO/MoS2/p-Si heterojunctions, ACS Appl. Mater. Interfaces 9 (21) (2017) 18377–18387.

[53] T. Kimoto, SiC material properties, in: Wide Bandgap Semiconductor Power Devices, Woodhead Publishing, 2019, pp. 21–42.

[54] W. Shockley, The Theory of p-n Junctions in Semiconductors and p-n Junction Transistors, Bell Syst. Tech. J. 28 (3) (1949) 435–489.

[55] S.O. Kasap, Electronic materials and Devices, McGraw-Hill New York, 2006.

[56] J.I. Pankove, Optical processes in semiconductors, Courier Corporation, 1975.

[57] C.Q. Yu, H. Wang, Large near-infrared lateral photovoltaic effect observed in Co/Si metal-semiconductor structures, Appl. Phys. Lett. 96 (17) (2010) 171102.

[58] Y. Zhang, Y. Zhang, T. Yao, C. Hu, Y. Sui, X. Wang, Ultrahigh position sensitivity and fast optical relaxation time of lateral photovoltaic effect in Sb 2 Se 3/p-Si junctions, Opt. Express 26 (26) (2018) 34214–34223.

[59] Z. Zhang, S. Qiao, J. Liu, L. Guo, Z. Li, L. Yang, G. Fu, Lateral photocurrent-induced high-performance self-powered photodetector observed in CIGS heterojunction, IEEE Trans. Electron Devices 67 (4) (2020) 1639–1644.

[60] B.K. Sarker, E. Cazalas, T.F. Chung, I. Childres, I. Jovanovic, Y.P. Chen, Position-dependent and millimetre-range photodetection in phototransistors with micrometre-scale graphene on SiC, Nat. Nanotechnol. 12 (7) (2017) 668–674.